Weierstraß-Institut

für Angewandte Analysis und Stochastik

Leibniz-Institut im Forschungsverbund Berlin e. V.

Preprint ISSN 0946 – 8633

Direct discretizations of bi-variate population balance systems with finite difference schemes of different order

Volker John [1,2], Carina Suciu [1]

submitted: September 30, 2013

[1] Weierstrass Institute
Mohrenstr. 39
10117 Berlin
Germany
email: Volker.John@wias-berlin.de
email: Carina.Suciu@wias-berlin.de

[2] Free University of Berlin
Department of Mathematics and Computer Science
Arnimallee 6
14195 Berlin
Germany

No. 1848
Berlin 2013

2010 *Mathematics Subject Classification.* 76T20.

Key words and phrases. bi-variate population balance systems; direct discretizations; finite difference methods; accuracy of numerical results.

Edited by
Weierstraß-Institut für Angewandte Analysis und Stochastik (WIAS)
Leibniz-Institut im Forschungsverbund Berlin e. V.
Mohrenstraße 39
10117 Berlin
Germany

Fax: +49 30 20372-303
E-Mail: preprint@wias-berlin.de
World Wide Web: http://www.wias-berlin.de/

Abstract

The accurate and efficient simulation of bi-variate population balance systems is nowadays a great challenge since the domain spanned by the external and internal coordinates is five-dimensional. This report considers direct discretizations of this equation in tensor-product domains. In this situation, finite difference methods can be applied. The studied model includes the transport of dissolved potassium dihydrogen phosphate (KDP) and of energy (temperature) in a laminar flow field as well as the nucleation and growth of KDP particles. Two discretizations of the coupled model will be considered which differ only in the discretization of the population balance equation: a first order monotone upwind scheme and a third order essentially non-oscillatory (ENO) scheme. The Dirac term on the right-hand side of this equation is discretized with a finite volume method. The numerical results show that much different results are obtained even in the class of direct discretizations.

1 Introduction

Population balance modeling has gained a lot of attention in the last few years, since many particulate processes can be described with its help, e.g., crystal-

lization, comminution, precipitation, polymerization, aerosol, and emulsion processes. In particular, population balance systems for crystallization processes model the interaction of the surrounding medium and particles, which are described by a particle size distribution (PSD). Moreover, this interaction leads to different phenomena, e.g., nucleation, growth, aggregation, breakage, and transport of particles [13,8]. Physical quantities in those systems, like temperature and concentrations, depend on time and so-called external coordinates, whereas the PSD depends on time, external coordinates, and so-called internal coordinates, which describe additional properties of the individual particles, e.g., diameter, volume, or main axes in case of anisotropic particles. Population balance systems take into account a flow field transporting the particles. This approach results in a system of partial differential equations where the Navier–Stokes equations for the fluid velocity and pressure are coupled to convection-diffusion equations for the concentration of the species and the temperature of the system and a transport equation for the PSD. The flow field, temperature field, and concentration field are defined in a three-dimensional domain while the PSD is defined in a higher-dimensional domain, spanned by the external and internal coordinates.

There are different goals of numerical simulations. One goal consists in gaining a deeper insight into physical processes (models) by such simulations. In this case, one should use accurate (high order) numerical methods. Of course, such methods are generally computational expensive. Another goal might be to utilize numerical simulations for a real time control of processes. In this situation, very efficient methods have to be applied. However, such methods are usually of low order, i.e., one has to expect only a low accuracy of the numerical results. Altogether, different goals of numerical simulations require the use of numerical methods with different properties and one should choose the method according to the goal. This report focuses on the accuracy of numerical methods. Main goals of this report consist, on the one hand, in increasing the sensitivity of the population balance community on the possible size of numerical errors and on the other hand, in motivating careful and systematic studies of the properties of numerical methods for solving multivariate population balance systems in order to obtain guidelines on which method is appropriate for which goal.

To this end, the crystallization process of potassium dihydrogen phosphate (KDP) is considered as bi-variate model, i.e., with two internal coordinates. Particle transport as well as temperature-dependent nucleation and growth are taken into account. The coupling is modeled as one-way coupling, which means that the flow field is used for the computation of concentration, temperature, and the PSD. The back coupling can be neglected in the used model because of a sufficiently small amount of particles, suspended in a dilute dispersion medium, and of the presence of sufficiently small temperature gradients.

The numerical solution of bi-variate population balance system is computationally challenging since the equation for the PSD is given in a five-dimensional domain in each discrete time. In order to overcome the increase in dimension, techniques based on model simplification are widely employed. One approach consists in replacing the higher-dimensional equation for the PSD by a system of equations for the first moments of the PSD, which is a system in three dimensions [13]. The most popular approaches in this direction are the quadrature method of moments (QMOM) [25] and nowadays the direct quadrature method of moments (DQMOM) [24]. The DQMOM has been used for the simulation of multi-variate population balance systems, e.g., in [4]. However, it is well known that the reconstruction of a PSD from a finite number of its moments is a severely ill-posed problem [14,5]. Other approaches consider directly the equation for the PSD, for instance, numerical methods based on operator-splitting techniques or direct discretizations (so-called discrete methods). The basic idea of operator-splitting techniques is to split the high-dimensional equation into two low-dimensional equations, one with respect to the external coordinates and one with respect to the internal coordinates, and solve them sequentially, e.g., see [7] for the use of such methods for the simulation of a crystallization process. However, this approach introduces splitting errors whose magnitude is known only in model situations [6]. With the increase of computational power, direct discretizations of the population balance equation become an interesting option. In these methods, the external and internal coordinates are discretized together, thus additional errors from simplifying the equation are not introduced. In this report, it will be shown that this approach is nowadays possible. To our best knowledge, the presented simulations are the first ones with direct discretizations for bi-variate population balance systems. Altogether, we think that among the numerical approaches mentioned here, potentially the most accurate simulations can be performed by using direct discretizations. For this reason, two methods from the class of direct discretizations will be studied.

This report focuses on the accuracy of the considered two methods from the class of direct discretizations. In both methods, the flow field is simulated with a higher order finite element method, the convection-dominated equations for temperature and concentration with a linear flux-corrected transport (FCT) finite element method, and the transport equation for the PSD with methods based on finite difference schemes. Both studied methods differ only in the concrete finite difference approximation: a first order monotone upwind scheme and a third order essentially non-oscillatory (ENO) scheme. In the considered setup, the five-dimensional domain spanned by the external and internal coordinates can be decomposed by a tensor-product mesh, which enables the utilization of finite difference methods for the differential operator on the left-hand side of the population balance equation. However, the right-hand side of this equation contains a Dirac distribution such that a finite difference approach cannot be applied for this term. In this report, a finite

volume method will be used for the right-hand side and it is explained in detail how the correct scaling has to be chosen to obtain finally a hybrid finite difference - finite volume discretization for the population balance equation.

The report is organized as follows. The studied process is described in Section 2. In Section 3, the system of equations modeling the bi-variate population balance system is introduced. A brief description of the numerical methods and the couplings within the population balance system is presented in Section 4. Section 5 constitutes the main part of this report, which includes comprehensive numerical studies and a discussion of the results. Finally, a summary and an outlook are given in Section 6.

2 The studied process

In the studied process, KDP is the solute and water is the solvent. KDP is a popular model substance for bi-variate crystal research. The shape of KDP crystals is a tetragonal prism in combination with tetragonal bi-pyramids [22], as illustrated in Fig. 1. The length of the crystal is given by $\tilde{L}_2$ and the width and depth are both equal to $\tilde{L}_1 \leq \tilde{L}_2$.

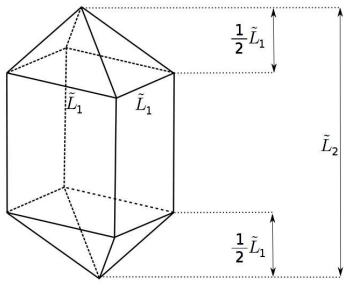

Fig. 1. Characteristic lengths of KDP crystals.

The volume of the crystal is given by

$$\tilde{V} = \frac{1}{3}\tilde{L}_1^3 + \left(\tilde{L}_2 - \tilde{L}_1\right)\tilde{L}_1^2. \tag{1}$$

The model parameters used in our simulations are based on experimental data from [1,3,28].

For the considered configuration, we do not possess measurement data, neither for an initial nor for a final particle size distribution. However, for the goals of this report, it is sufficient to use some kind of realistic data sets and to demonstrate the impact of different methods on the obtained numerical results. The flow domain is a channel of the same size as in [10]. Note that the simulations from [10] are based on experiments such that data sets taken as in, or similar to, [10] represent realistic situations. At the inlet, equally distributed seed

particles of prescribed lengths within a rather narrow interval of both lengths are chosen. The inlet of particles occurs only for a short time interval. Then, the particles are transported from the inlet to the outlet of the channel. The flow fields are almost the same as in [10], only the solvent ethanol in [10] is here replaced by water. During the residence time in the channel, the particles grow and new particles are created by nucleation in supersaturated solution. Growth and nucleation depend on the temperature. The data for the temperature field and the concentration field (initial and boundary conditions) are computed or chosen the same way as in [10]. Aggregation of particles is not included into the model for two reasons. First, one would need some model on how to classify the aggregate of two particles of the from presented in Fig. 1 within the framework of the considered bi-variate population. And second, to our best knowledge, predictive models for aggregation kernels for bi-variate populations are not known so far.

Outputs of interest are the form of the PSD and its maximal value in three planes perpendicular to the flow direction: one rather close to the inlet, one at around one fourth of the length of the channel, and the last one at the outlet.

3 The model for the population balance system

The population of KDP crystals is modeled by a system of equations describing the flow field (velocity, pressure), the energy balance (temperature), the mass balance (concentration), and the particle size distribution. Secondary nucleation, growth, and transport of the particles are taken into account.

Based on the experimental setup from [2] and the simulations from [10], the flow field will be described by the incompressible steady-state Navier–Stokes equations

$$\begin{aligned} -\mu\Delta\tilde{\mathbf{u}} + \rho\left((\tilde{\mathbf{u}}\cdot\nabla)\tilde{\mathbf{u}}\right) + \nabla\tilde{p} &= \rho\tilde{\mathbf{g}} \quad \text{in } \tilde{\Omega}, \\ \nabla\cdot\tilde{\mathbf{u}} &= 0 \quad \text{in } \tilde{\Omega}, \end{aligned} \tag{2}$$

where $\tilde{\Omega} = (0, 210)\times(0, 1)\times(0, 1)$ cm^3 is the flow domain, $\mu = 1.5{\cdot}10^{-3}$ kg/(ms) is the dynamic viscosity of the overall solution at 298 K, $\rho = 1160$ kg/m^3 is density of the overall solution at 298 K, and $\tilde{\mathbf{g}}$ $[m/s^2]$ is the gravitational acceleration. The functions to be simulated are the fluid velocity $\tilde{\mathbf{u}}$ [m/s] and the pressure p [Pa]. Since the process is set up in such a way that the suspension is sufficiently dilute, the size of the particles is sufficiently small, and the temperature gradient is also small enough, the influence of all these aspects on the flow field can be neglected. The Navier–Stokes equations (2) has to be equipped with boundary conditions. The boundary is given by $\tilde{\Gamma} = \tilde{\Gamma}_{\text{in}} \cup \tilde{\Gamma}_{\text{out}} \cup \tilde{\Gamma}_{\text{wall}}$, with $\tilde{\Gamma}_{\text{in}} = \{0 \text{ cm}\} \times (1/3 \text{ cm}, 2/3 \text{ cm}) \times (1/3 \text{ cm}, 2/3 \text{ cm})$ as the inlet boundary, $\tilde{\Gamma}_{\text{out}} = \{210 \text{ cm}\} \times (0 \text{ cm}, 1 \text{ cm}) \times (0 \text{ cm}, 1 \text{ cm})$ as the

outlet boundary, and $\tilde{\Gamma}_{\text{wall}} = \Gamma \setminus (\Gamma_{\text{in}} \cup \Gamma_{\text{out}})$ as the boundary at the walls. Analogously as in [10], it is assumed that only the flow rate at the inlet $\tilde{\Gamma}_{\text{in}}$ is known from an experiment. The construction of a continuous boundary condition at the plane where the inlet is situated, which matches a prescribed flow rate, is described in [10]. It has the form

$$\tilde{\mathbf{u}}(\tilde{\mathbf{x}}) = U_{\text{in}}(\Psi(\xi(\tilde{\mathbf{x}}), \eta(\tilde{\mathbf{x}})), 0, 0)^T, \quad \tilde{\mathbf{x}} \in \tilde{\Gamma}_{\text{in}},$$

where the profile $\Psi(\xi, \eta)$ is the solution of the two-dimensional Poisson equation

$$-\Delta\Psi = 1 \text{ in } \tilde{\Gamma}_{\text{in}}, \quad \Psi = 0 \text{ on } \partial\tilde{\Gamma}_{\text{in}}.$$

The parameter U_{in} is chosen to match the given inflow rates . The boundary condition at the outlet $\tilde{\Gamma}_{\text{out}}$ is the standard do-nothing condition,

$$(\mu\nabla(\tilde{\mathbf{u}}) - \tilde{p}\mathbb{I}) \cdot \tilde{\mathbf{n}}_{\tilde{\Gamma}} = \mathbf{0}, \quad \tilde{\mathbf{x}} \in \tilde{\Gamma}_{\text{out}}, \tag{3}$$

where $\tilde{\mathbf{n}}_{\tilde{\Gamma}}$ is the unit outer normal on $\tilde{\Gamma}$. A boundary condition at the outlet is often not known from experiments. In particular it is unclear how good this boundary condition corresponds to (3). For this reason, the computational domain should be somewhat larger than the actual domain such that a possible slight incorrectness of the outflow boundary condition (3) has no impact on the computational results in the region that corresponds to the outlet of the actual domain. In this report, this aspect is taken into account by studying $\tilde{x} = 200$ cm as outlet plane. At all other boundaries (the walls), the no-slip condition

$$\tilde{\mathbf{u}}(\tilde{\mathbf{x}}) = \mathbf{0}, \quad \tilde{\mathbf{x}} \in \tilde{\Gamma}_{\text{wall}},$$

is applied.

The mass balance of the KDP system is modeled by

$$\frac{\partial\tilde{c}}{\partial\tilde{t}} - D\Delta\tilde{c} + \tilde{\mathbf{u}} \cdot \nabla\tilde{c} = \frac{\tilde{\sigma}_{\text{gr}}}{m_{\text{mol}}} \text{ in } (0, \tilde{t}_{\text{end}}) \times \tilde{\Omega}, \tag{4}$$

where $\tilde{c}\,[kg/m^3]$ is the concentration of the solute, $\tilde{\sigma}_{\text{gr}}$ $[\text{kg}/(\text{m}^3\text{s})]$ is the mass transferred from the suspension to the solid phase due to the growth per unit time and unit space, $m_{\text{mol}} = 136.08 \cdot 10^{-3}$ kg/mol is the molar mass of KDP, and $D = 5.5 \cdot 10^{-10}$ m^2/s is the diffusion coefficient of KDP in water. The consumption of the solute by the growth of particles is modeled by the term on the right-hand side in (4)

$$\tilde{\sigma}_{\text{gr}} = -\rho^d \int_{\tilde{L}_{2,\min}}^{\tilde{L}_{2,\max}} \int_{\tilde{L}_{1,\min}}^{\min\{\tilde{L}_2, \tilde{L}_{1,\max}\}} \left(2\tilde{G}_1(\tilde{L}_1\tilde{L}_2 - \tilde{L}_1^2) + \tilde{G}_2\tilde{L}_1^2\right) \times \tilde{f}(\tilde{t}, \tilde{\mathbf{x}}, \tilde{L}_1, \tilde{L}_2)\, d\tilde{L}_1 d\tilde{L}_2, \tag{5}$$

with $\tilde{L}_{1,\min} = \tilde{L}_{2,\min} = 0$ m, $\tilde{L}_{1,\max} = 1200 \cdot 10^{-6}$ m, and $\tilde{L}_{2,\max} = 4000 \cdot 10^{-6}$ m. The growth rates for the individual internal coordinates are given by

$$\tilde{G}_i(\tilde{c}, \tilde{T}) = \begin{cases} k_{g_i} \left(\dfrac{\tilde{c} - \tilde{c}_{\text{sat}}(\tilde{T})}{\tilde{c}_{\text{sat}}(\tilde{T})} \right)^{g_i} & \text{if } \tilde{c} > \tilde{c}_{\text{sat}}(\tilde{T}), \\ 0 & \text{else,} \end{cases} \quad i = 1, 2,$$

with the model parameters $\rho^d = 2338$ kg/m^3 as the density of KDP (dispersed phase), $k_{g_1} = 1.221 \cdot 10^{-5}$ m/s as growth rate constant with respect to $\tilde{L}_1$, $k_{g_2} = 10.075 \cdot 10^{-5}$ m/s as growth rate constant with respect to $\tilde{L}_2$, $g_1 = 1.48$ $[\cdot]$ as growth rate power with respect to $\tilde{L}_1$, and $g_2 = 1.74$ $[\cdot]$ as growth rate power with respect to $\tilde{L}_2$. Equation (4) has to be equipped with initial and boundary conditions. The boundary condition is given by

$$\begin{cases} \tilde{c}(\tilde{t}, \tilde{\mathbf{x}}) = \tilde{c}_{\text{sat}}(\tilde{T}), \ \tilde{\mathbf{x}} \in \tilde{\Gamma}_{\text{in}}, \\ D \dfrac{\partial \tilde{c}}{\partial \tilde{\mathbf{n}}_{\tilde{\Gamma}}} = 0, \qquad \tilde{\mathbf{x}} \in \tilde{\Gamma}_{\text{out}} \cup \tilde{\Gamma}_{\text{wall}}, \end{cases}$$

with the saturation concentration taken as in [23]

$$\tilde{c}_{\text{sat}}(\tilde{T}) = \frac{9.3027\ 10^{-5} \tilde{T}^2 - 9.7629\ 10^{-5} \tilde{T} + 0.2087}{m_{\text{mol}}},$$

where $\tilde{T}$ $[K]$ is the temperature of the system. With this boundary condition, equation (4) without the coupling term to the PSD is solved until a steady state is reached. This steady state is used as initial condition

$$\tilde{c}(0, \tilde{\mathbf{x}}) = \tilde{c}_{\text{steady}}(\tilde{\mathbf{x}}).$$

Next, the energy balance of the KDP system is modeled by

$$\rho c_p \left(\frac{\partial \tilde{T}}{\partial t} + \mathbf{u} \cdot \nabla \tilde{T} \right) - \lambda \Delta \tilde{T} = \Delta h_{\text{cryst}} \tilde{\sigma}_{\text{gr}} \text{ in } (0, \tilde{t}_{\text{end}}) \times \tilde{\Omega}, \tag{6}$$

where $c_p = 4181.3$ J/(kg K) is the specific heat capacity of water, $\lambda = 0.602$ J/(K m s) is the thermal conductivity of water, and $\Delta h_{\text{cryst}} = 119$ J/kg is the heat of solution (enthalpy change of solution). The decrease of temperature with respect to the growth of the particles is modeled by the term on the right-hand side of (6), where $\tilde{\sigma}_{\text{gr}}$ is defined as in (5). The boundary conditions are given by

$$\begin{cases} \tilde{T}(\tilde{t}, \tilde{\mathbf{x}}) = 308.15\ K, \ \tilde{\mathbf{x}} \in \tilde{\Gamma}_{\text{in}}, \\ \lambda \dfrac{\partial \tilde{T}}{\partial \tilde{\mathbf{n}}_{\tilde{\Gamma}}} = 0, \qquad \tilde{\mathbf{x}} \in \tilde{\Gamma}_{\text{out}}, \\ \tilde{T}(\tilde{t}, \tilde{\mathbf{x}}) = 291.15\ K, \ \tilde{\mathbf{x}} \in \tilde{\Gamma}_{\text{wall}}. \end{cases}$$

Hence, the suspension is cooled at the wall. As initial condition, a fully developed temperature field, based on the solution of a steady-state equation without the coupling term to the PSD, is chosen

$$\tilde{T}(0,\tilde{\mathbf{x}}) = \tilde{T}_{\text{steady}}(\tilde{\mathbf{x}}).$$

Finally, the population balance equation for the bi-variate model is given by

$$\begin{aligned}\frac{\partial \tilde{f}}{\partial \tilde{t}} + \tilde{G}_1(\tilde{c},\tilde{T})\frac{\partial \tilde{f}}{\partial \tilde{L}_1} + \tilde{G}_2(\tilde{c},\tilde{T})\frac{\partial \tilde{f}}{\partial \tilde{L}_2} + \tilde{\mathbf{u}}\cdot\nabla\tilde{f} = \tilde{H}_{\text{nuc}} \\ \text{in } (0,\tilde{t}_{\text{end}})\times\tilde{\Omega}\times(\tilde{L}_{1,\min},\tilde{L}_{1,\max})\times(\tilde{L}_{2,\min},\tilde{L}_{2,\max}).\end{aligned} \tag{7}$$

The right-hand side in (7) accounts for nucleation which is assumed to occur at the smallest particles

$$\tilde{H}_{\text{nuc}} = \tilde{B}_{\text{nuc}}(\tilde{c},\tilde{T})\tilde{V}_{cryst}\delta(\tilde{L}_1-\tilde{L}_{1,\text{nuc}})\delta(\tilde{L}_2-\tilde{L}_{2,\text{nuc}}), \tag{8}$$

with δ being the Dirac delta distribution,

$$\delta(\tilde{L}_i-\tilde{L}_{i,\text{nuc}}) = \begin{cases}1 & \text{if } \tilde{L}_i = \tilde{L}_{i,\text{nuc}},\\ 0 & \text{else,}\end{cases} \qquad i=1,2,$$

with $\tilde{L}_{1,\text{nuc}} = 50\cdot 10^{-6}$ m and $\tilde{L}_{2,\text{nuc}} = 100\cdot 10^{-6}$ m. This model for the nucleation is standard and it has been proposed, e.g., in [1]. The volume for the crystalline phase can be computed by

$$\tilde{V}_{\text{cryst}} = \int_{\tilde{L}_{2,\min}}^{\tilde{L}_{2,\max}}\int_{\tilde{L}_{1,\min}}^{\min\{\tilde{L}_2,\tilde{L}_{1,\max}\}} \tilde{V}\tilde{f}\; d\tilde{L}_1 d\tilde{L}_2,$$

where $\tilde{V}$ is given in (1), and the nucleation rate is defined by

$$\tilde{B}_{\text{nuc}}(\tilde{c},\tilde{T}) = \begin{cases} k_b\left(\dfrac{\tilde{c}-\tilde{c}^c_{\text{sat}}(\tilde{T})}{\tilde{c}^c_{\text{sat}}(\tilde{T})}\right)^b & \text{if } \tilde{c} > \tilde{c}^c_{\text{sat}}(\tilde{T}),\\ 0 & \text{else,}\end{cases}$$

with the model parameters $k_b = k_{\text{nuc}}\cdot V_{\text{overall}}$ $[1/(\text{m}^3\text{s})]$ with $k_{\text{nuc}} = 3.75\cdot 10^{13}$ $1/(\text{m}^6\text{s})$, $V_{\text{overall}} = 2.1\cdot 10^{-4}\text{m}^3$ (volume of the channel), and $b = 2.04$ $[\cdot]$ as the nucleation rate power. The initial condition is given by

$$\tilde{f}(0,\tilde{\mathbf{x}},\tilde{L}_1,\tilde{L}_2) = 0 \quad \text{in } \tilde{\Omega}\times(\tilde{L}_{1,\min},\tilde{L}_{1,\max})\times(\tilde{L}_{2,\min},\tilde{L}_{2,\max}),$$

i.e., there are no particles in the flow domain. Boundary conditions are neces-

sary on the closure of the inflow boundaries

$$\tilde{f}(\tilde{t}, \tilde{\mathbf{x}}, \tilde{L}_1, \tilde{L}_2) = \begin{cases} \tilde{f}_{\text{in}}(\tilde{t}, \tilde{\mathbf{x}}, \tilde{L}_1, \tilde{L}_2), \ \tilde{\mathbf{x}} \in \tilde{\Gamma}_{\text{in}}, \tilde{t} \in [0, \tilde{t}_{\text{inj}}] \text{ s}, \\ 0, \qquad\qquad\qquad \text{else}, \end{cases}$$

where $\tilde{f}_{\text{in}}$ is given by, see Fig. 2,

$$\tilde{f}_{\text{in}}(\tilde{t}, \tilde{\mathbf{x}}, \tilde{L}_1, \tilde{L}_2) = \begin{cases} 1, & \text{if } \tilde{L}_1 \in (150, 250) \cdot 10^{-6} \text{ m}, \ \tilde{L}_2 \in (600, 1000) \cdot 10^{-6} \text{ m}, \\ 0, & \text{else}, \end{cases}$$

for $\tilde{t} \in [0, \tilde{t}_{\text{inj}}]$ s with $\tilde{t}_{\text{inj}} = 10$ s.

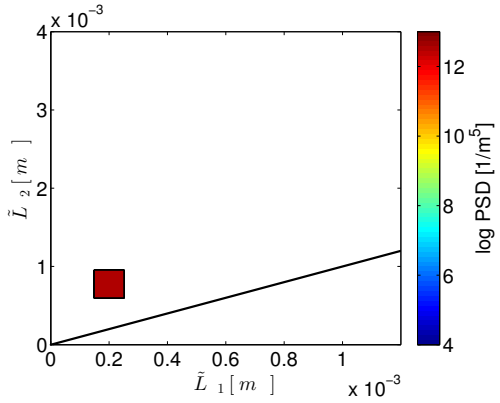

Fig. 2. Equally distributed seed PSD at the inlet of the channel for $\tilde{t} \in [0, \tilde{t}_{\text{inj}}]$ s.

Numerical simulations are based on dimensionless equations. In our numerical studies, the following reference values are used for deriving these equations: $f_\infty = 10^{13}$ 1/m^5, $l_\infty = 0.01$ m, $u_\infty = 0.01$ m/s, $T_\infty = 1$ K, $c_\infty = 1$ mol/m^3, $L_{1,\infty} = 1000 \cdot 10^{-6}$ m, and $L_{2,\infty} = 1000 \cdot 10^{-6}$ m.

4 Numerical methods

The model of the population balance system presented in Section 3 results in a system of partial differential equations where the Navier–Stokes equations for the fluid velocity and pressure are coupled to convection-diffusion equations for the species concentration and the system temperature and a transport equation for the particle size distribution. The last three equations are coupled mutually. All spatial discretizations are performed on a hexahedral grid.

For the considered flow rates, it turns out that the Navier–Stokes equations (2) admit a stable steady-state solution. Since the computation of the velocity $\mathbf{u}$ and the pressure p does not require any information from temperature (T), concentration (c), and PSD (f), the steady-state flow field is computed in

a preprocessing step. For discretizing this equation, the inf-sup stable pair of finite element spaces Q_2/P_1^{disc} is applied, which is considered to be an accurate choice, e.g., see [9].

Both equations for the temperature and the concentration are time-dependent and strongly convection-dominated. Therefore, apart from the spatial discretization, a discretization in time is also required. To this end, the Crank–Nicolson scheme is applied. In space, the Q_1 finite element is used. Due to the dominant convection, a stabilized finite element has to be applied. Here, a linear flux-corrected transport (FEM-FCT) method is used, which is a variant of a method proposed in [21]. The combination of this method and the Crank–Nicolson scheme has been proved to be one of the best performing, with respect to the ratio of accuracy and efficiency, finite element methods in competitive studies [19,20,17].

Altogether, the equations that are defined in the physical domain only are discretized with accurate finite element methods that are state of the art.

Since the domain $\tilde{\Omega}$ is of tensor-product form, the domain spanned by the external and internal coordinates can be decomposed by a tensor-product mesh. Such a mesh enables the utilization of finite difference methods. Finite difference methods are comparatively cheap methods. In competitive studies [17] it has been shown that they are superior, with respect to the ratio of accuracy and efficiency, to finite element methods in the tensor-product setting. However, the usual application of finite difference methods to (7) becomes impossible due to the Dirac distribution contained in the right-hand side (8), because for finite difference methods, the right-hand side must be a continuous function. But the Dirac distribution can be discretized with finite volume methods since the integral of this distribution is well defined.

Thus, in the numerical simulations, a hybrid discretization is utilized that uses for the left-hand side of (7) finite difference methods and for the right-hand side a finite volume method. Let $\Omega_L = [L_{1,\min}, L_{1,\max}] \times [L_{2,\min}, L_{2,\max}]$. This domain is decomposed by cells

$$K_{i,j} = \left[L_{1,i-1/2}, L_{1,i+1/2}\right] \times \left[L_{2,j-1/2}, L_{2,j+1/2}\right], \quad 1 \le i \le N_{L_1}, 1 \le j \le N_{L_2},$$

with $L_{i,\min} = L_{i,1/2} \le L_{i,3/2} \le \cdots \le L_{i,N_{L_i}+1/2} = L_{i,\max}$, $i = 1, 2$. Denote by $(L_{1,i}, L_{2,j})$ the barycenter of $K_{i,j}$ and by $\Delta L_{1,i} = L_{1,i+1/2} - L_{1,i-1/2}$, $\Delta L_{2,j} = L_{2,j+1/2} - L_{2,j-1/2}$ its edge sizes. The finite volume formulation of (7) with respect to the internal coordinates for the cell $K_{i,j}$ reads [12]

$$\int_{K_{i,j}} \mathbf{G} \cdot \nabla_L f \; dL_1 dL_2 = \int_{K_{i,j}} H_{\text{nuc}} \; dL_1 dL_2, \tag{9}$$

with

$$\mathbf{G} = \begin{pmatrix} G_1 \\ G_2 \end{pmatrix}, \quad \nabla_L f = \begin{pmatrix} \frac{\partial f}{\partial L_1} \\ \frac{\partial f}{\partial L_2} \end{pmatrix}, \quad H_{\text{nuc}} = C_{\text{nuc}} \delta(L_1 - L_{1,\text{nuc}}) \delta(L_2 - L_{2,\text{nuc}}),$$

where C_{nuc} comprises the parameters from (8) and the factor coming from deriving the dimensionless equations. Applying the Gaussian divergence theorem to (9) and using the fact that $\nabla_L \cdot \mathbf{G} = 0$ yields

$$\begin{aligned} \int_{\Gamma_{K_{i,j}}} (\mathbf{G} \cdot \mathbf{n}_{K_{i,j}}) f \, d\Gamma_L &= C_{\text{nuc}} \int_{K_{i,j}} \delta(L_1 - L_{1,\text{nuc}}) \delta(L_2 - L_{2,\text{nuc}}) \, dL_1 dL_2 \\ &= C_{\text{nuc}} \begin{cases} 1 & \text{if } (L_{1,\text{nuc}}, L_{2,\text{nuc}}) \in K_{i,j}, \\ 0 & \text{else,} \end{cases} \\ &=: C_{\text{nuc},\delta_{ij}}, \end{aligned} \tag{10}$$

where $\mathbf{n}_{K_{i,j}}$ is the unit outward normal vector to $\Gamma_{K_{i,j}}$. The left-hand side in (10) is discretized by applying the midpoint rule on the edges of $K_{i,j}$, leading to

$$\begin{aligned} &\int_{\Gamma_{K_{i,j}}} (\mathbf{G} \cdot \mathbf{n}_{K_{i,j}}) f \, d\Gamma_L \\ &\approx G_1 \Delta L_{2,j} \left(f^h_{i+1/2,j} - f^h_{i-1/2,j} \right) + G_2 \Delta L_{1,i} \left(f^h_{i,j+1/2} - f^h_{i,j-1/2} \right). \end{aligned}$$

Thus, the finite volume discretization of (9) becomes

$$G_1 \Delta L_{2,j} \left(f^h_{i+1/2,j} - f^h_{i-1/2,j} \right) + G_2 \Delta L_{1,i} \left(f^h_{i,j+1/2} - f^h_{i,j-1/2} \right) = C_{\text{nuc},\delta_{ij}}. \tag{11}$$

Multiplying this equation by $1/(\Delta L_{1,i} \Delta L_{2,j})$, one gets

$$G_1 \frac{\left(f^h_{i+1/2,j} - f^h_{i-1/2,j} \right)}{\Delta L_{1,i}} + G_2 \frac{\left(f^h_{i,j+1/2} - f^h_{i,j-1/2} \right)}{\Delta L_{2,j}} = \frac{C_{\text{nuc},\delta_{ij}}}{\Delta L_{1,i} \Delta L_{2,j}}, \tag{12}$$

which is the central finite volume discretization. This type of discretization might lead to spurious oscillations in the numerical solutions in the case that convection dominates. Then, other types of finite volume schemes are used, e.g., schemes of upwind type. Applying the standard upwind technique to (12) yields the upwind finite volume scheme

$$G_1 \frac{\left(f^h_{i,j} - f^h_{i-1,j} \right)}{\Delta L_{1,i}} + G_2 \frac{\left(f^h_{i,j} - f^h_{i,j-1} \right)}{\Delta L_{2,j}} = \frac{C_{\text{nuc},\delta_{ij}}}{\Delta L_{1,i} \Delta L_{2,j}}, \tag{13}$$

for $G_1 \geq 0$ and $G_2 \geq 0$. Now, one can observe that the left-hand side of (13) coincides with the upwind finite difference discretization of the convective term with respect to the internal coordinates of the left-hand side in (7). This correlation provides the link between applying a finite difference method for discretizing the left-hand side of (7) and a finite volume method for discretizing the right-hand side of (7): the right-hand side of the finite volume discretization (11) has to be multiplied with the scaling factor $1/(\Delta L_{1,i} \Delta L_{2,j})$ to become the correctly scaled right-hand side for a discretization with a finite difference operator on the left-hand side.

The last important component of the numerical method is the solution of the nonlinear coupled system consisting of the equations for temperature, concentration, and PSD. This system is solved iteratively with a fixed point iteration where one iteration consists of three steps:

- solve the equation for temperature with the currently available approximations of the concentration and the PSD;
- solve the equation for concentration with the approximation of the temperature computed in the first step and the currently available approximation of the PSD;
- solve the equation for PSD with the approximations of the temperature and concentration computed in the first two steps.

The iteration for solving the coupled system is stopped if the sum of the Euclidean norms of the residual vectors for concentration and temperature is below a prescribed tolerance.

The main topic of the numerical studies will be the finite difference discretization for the left-hand side of (7). On the one hand, a popular low order method is used, which consists of the forward Euler discretization for the temporal derivative and the simple upwind discretization for the derivatives with respect to the external and internal coordinates. This first order approach has been applied in our work so far [16,18,10]. For sufficiently small time steps, this method is monotone, i.e., the numerical solution does not possess spurious oscillations, like negative values for the PSD. A detailed description of this method can be found in [18]. The second discretization studied in this report is a total variation diminishing (TVD) Runge–Kutta method for the temporal derivative in combination with an essentially non-oscillatory (ENO) scheme for the derivatives with respect to external and internal coordinates [11,26]. This discretization is of third order. It is, as the name already suggests, only essentially monotone. Thus, small spurious oscillations might sometimes occur, as seen, e.g., in the numerical studies of [17]. In this paper, one can find a detailed description of this method. To our best knowledge, this method has not been used in the direct discretization of bi-variate population balances systems so far.

5 Numerical studies

The numerical studies consider two numerical methods for simulating the population balance system from Section 3. These methods differ only in one component, namely the discretization of the left-hand side of the PSD equation (7), where a forward Euler scheme with an upwind finite difference discretization (FWE-UPW-FDM) and a TVD Runge–Kutta method combined with an ENO finite difference discretization (RK-ENO-FDM) are used. The main focus is on the differences in accuracy of the computed results. In a first study, a flow field with inflow rate 30 ml/min will be considered. After having evaluated the results for this configuration in detail, results obtained for a configuration with inflow rate 90 ml/min will be discussed briefly. For simplicity of notation, the whole numerical methods for simulating the population balance system are abbreviated by FWE-UPW-FDM and RK-ENO-FDM, respectively.

The flow domain is long compared with its thickness and there is a preferred direction of the flow, which enables the use of an a priori adapted and anisotropic grid of $132 \times 12 \times 12$ cells, see [10] for details. For the internal coordinates, a uniform mesh was used with 25 nodes with respect to the smaller length of the particles, $\tilde{L}_1$, and 81 nodes with respect to the larger length of the particles, $\tilde{L}_2$. The corresponding numbers of degrees of freedom for simulating the population balance system are given in Table 1.

Table 1
Degrees of freedom for simulating the population balance system.

Simulation quantity	Number of d.o.f.
velocity	496 875
pressure	76 032
temperature	22 477
concentration	22 477
PSD	45 515 925

To highlight the differences of the results obtained with both methods, the PSD was studied at different locations in the channel. To this end, three cut planes are chosen, one close to the inlet at $\tilde{x}_1 = 17.5$ cm, one more downstream at $\tilde{x}_1 = 49$ cm, and the last one close to the outlet at $\tilde{x}_1 = 200$ cm, see Fig. 3.

5.1 Inflow rate 30 ml/min

In the first numerical study, a flow rate of $\tilde{V}_r = 30$ ml/min at the inlet was considered. The stationary flow field at the inlet of the channel is shown in

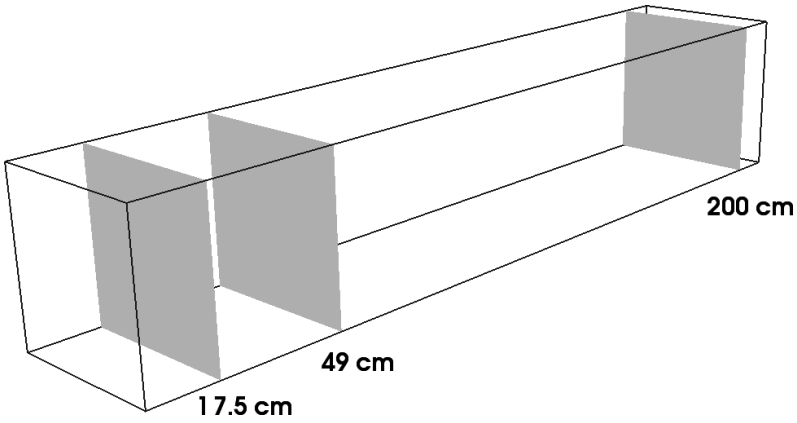

Fig. 3. Cut planes, parallel to the plane $\tilde{x}_1 = 0$, for comparing the results obtained with the two numerical schemes.

Fig. 4. Based on the mean velocity at the inlet (4.5 cm/s), the kinematic viscosity of the fluid, and the height of the channel (0.01 m), the Reynolds number of the flow is $Re \approx 348$.

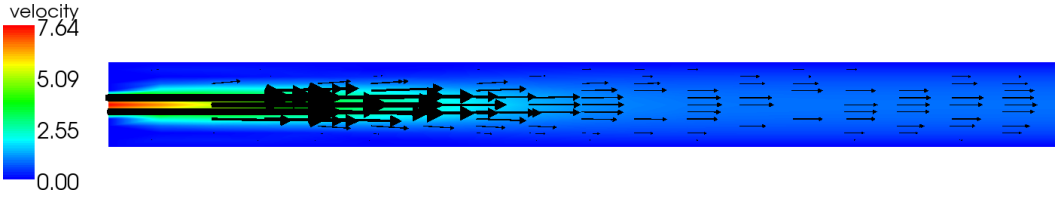

Fig. 4. Inflow rate $\tilde{V}_r = 30$ ml/min, the stationary velocity field at the inlet of the channel in a cut plane, domain not to scale.

At the beginning of the process, in the time interval $\tilde{t}_{\text{inj}} \in [0, 10]$ s, seed particles are injected into the channel, see Fig. 2 for the initial PSD. It turns out that almost all particles had left the domain after $\tilde{t} = 300$ s, such that the simulations are performed in the (dimensionless) time interval $[0, 300]$.

First, an appropriate time step has to be found. If the time step is too large, instabilities have to be expected because explicit time-stepping schemes are applied. If the time step is too small, then the simulation is inefficient. In addition, from our experience, we expected that for sufficiently small time steps the discretization error with respect to the external and internal coordinates dominates, and therefore a further decrease of the time step does not lead to an increase of the accuracy of the results. To find possible instabilities, the PSD in the center of the channel at the plane close to the inlet, at $(\tilde{x}_1, \tilde{x}_2, \tilde{x}_3) = (17.5, 1/2, 1/2)$ cm, is studied, see Fig. 5. Up to this point, there is more or less only a transport of the initial PSD. In particular, one does not expect values that are much larger than the maximal value of the initial PSD, which is 10^{13}. It can be seen in Fig. 5, upper pictures, that such values are computed for $\Delta t = 0.2$ (both schemes) and $\Delta t = 0.15$ (RK-ENO-FDM). The lower pictures of Fig. 5 reveal that for both schemes the results for $\Delta t \leq 0.1$ are very similar. From Fig. 6, it can be observed that this statement holds

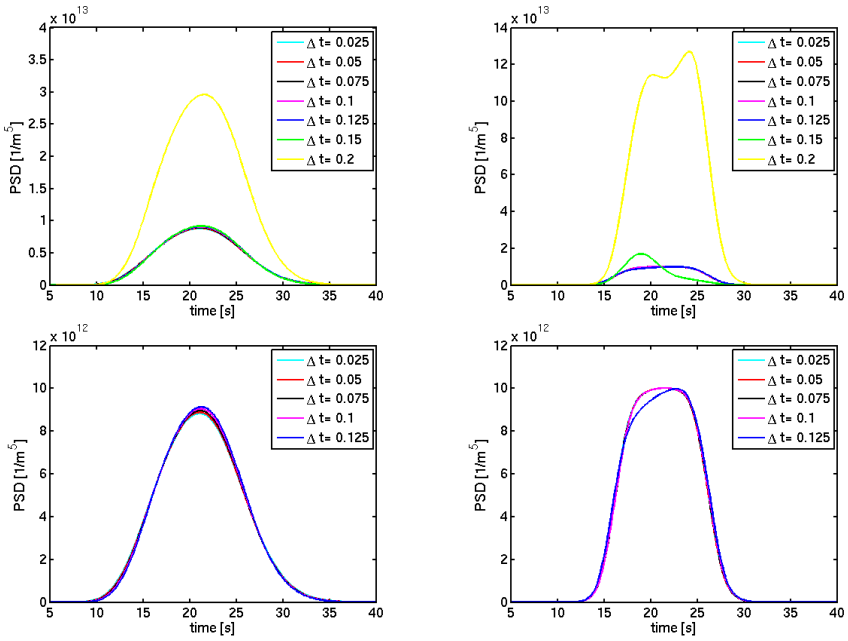

Fig. 5. Inflow rate $\tilde{V}_r = 30$ ml/min: maximal value of the PSD at $(\tilde{x}_1, \tilde{x}_2, \tilde{x}_3) = (17.5, 1/2, 1/2)$ cm for different time steps, FWE-UPW-FDM (left), RK-ENO-FDM (right). Note the different scaling of the y-axes.

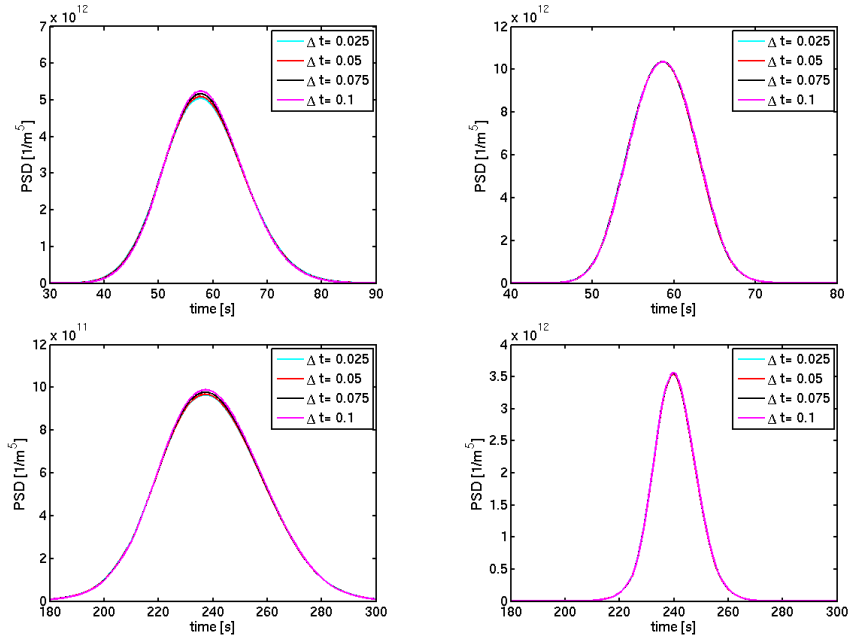

Fig. 6. Inflow rate $\tilde{V}_r = 30$ ml/min: maximal value of the PSD for different time steps, FWE-UPW-FDM (left); RK-ENO-FDM (right), $(\tilde{x}_1, \tilde{x}_2, \tilde{x}_3) = (49, 1/2, 1/2)$ cm (top), $(\tilde{x}_1, \tilde{x}_2, \tilde{x}_3) = (200, 1/2, 1/2)$ cm (bottom). Note the different scaling of the y-axes.

true also for the other cut planes. Therefore, $\Delta t = 0.1$ satisfies the conditions for an appropriate length of the time step and only results obtained with this

length will be presented in the detailed discussion.

For a detailed evaluation of the computational results, the temporal evolution of the PSD was studied not only at the center of the cut planes shown in Fig. 3, but also at other points situated in these planes. These points are sketched in Fig. 7. There is one set of points reaching from the center of the channel to the center of a lateral wall and another set, where the points reach from the center to the corner of two lateral walls. Due to the different velocities in all these points, a different evolution of the PSD can be expected.

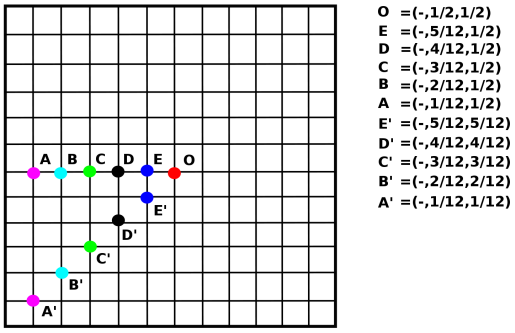

Fig. 7. Studied nodes for the cut planes parallel to the plane $\tilde{x}_1 = 0$.

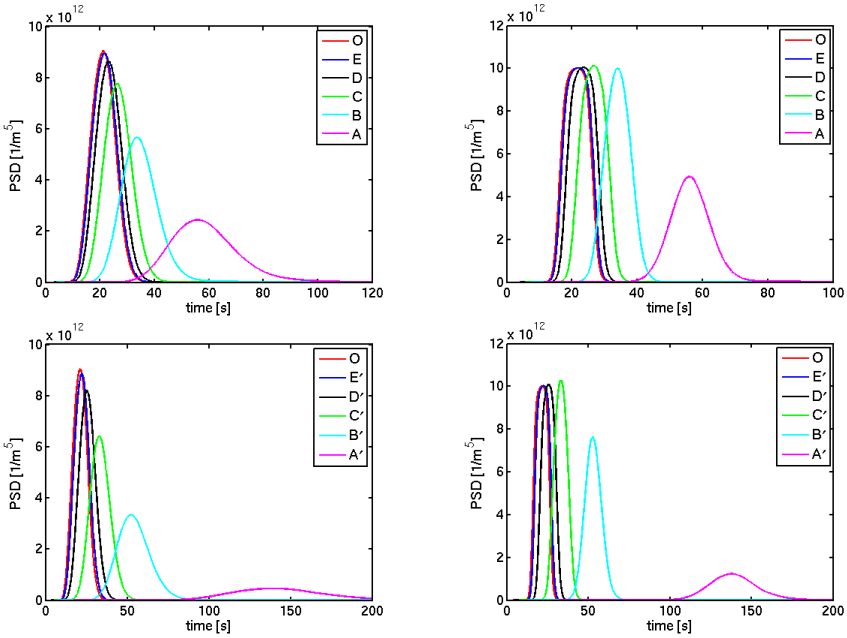

Fig. 8. Inflow rate $\tilde{V}_r = 30$ ml/min: maximal value of the PSD at different nodes $(17.5, \tilde{x}_2, \tilde{x}_3)$ cm, FWE-UPW-FDM (left); RK-ENO-FDM (right). Note the different scaling of the y-axes.

To keep the presentation of the results concise, only the evolution of the maximal value of the PSD in these points in the first and last cut plane will be presented, see Figs. 8 and 9. It can be seen that the largest maximal values are predicted in the center of the channel, i.e., the bulk of particles follows the

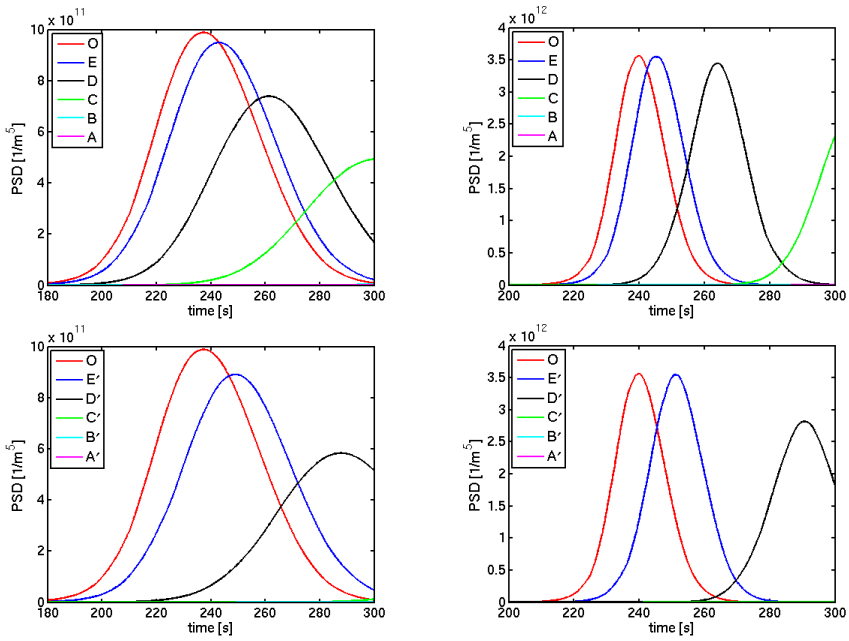

Fig. 9. Inflow rate $\tilde{V}_r = 30$ ml/min: maximal value of the PSD at different nodes $(200, \tilde{x}_2, \tilde{x}_3)$ cm, FWE-UPW-FDM (left), RK-ENO-FDM (right). Note the different scaling of the x- and y-axes. Maximal values of the PSD in the nodes with a distance less than or equal to 1/6 cm of one of the walls are negligible (magenta and cyan curves).

flow very well. The further the point of observation is away from the center, the smaller the maximal value of the PSD becomes. This general qualitative behavior is predicted by both of the studied schemes, FWE-UPW-FDM and RK-ENO-FDM. However, the height of the peaks (highest amount of particles that can be observed at the point at a certain time) and the time interval where the curve is clearly larger than zero (time interval where a notable number of particles can be observed at the point) often differ considerably between both methods. One can observe that the differences in the numerical results are the larger, the further the cut plane is away from the inlet, i.e., the longer the particles needed to reach the cut plane. Always, the method FWE-UPW-FDM gives results with smaller peaks and larger time intervals in which particles can be observed. Already close to the inlet, at the plane $\tilde{x} = 17.5$ cm, notable differences can be seen. At the outlet, the differences are very large. As an example, at the center of the channel $(\tilde{x}_1, \tilde{x}_2, \tilde{x}_3) = (200, 1/2, 1/2)$ cm, the method FWE-UPW-FDM predicts a notable amount of particles in the time interval $[190, 290]$ s, whereas RK-ENO-FDM shows this event in $[215, 265]$ s, thus the lengths of the respective time intervals are 100 s and 50 s. Moreover, the maximal amount of particles computed by RK-ENO-FDM is almost four times larger than the prediction of FWE-UPW-FDM.

Comprehensive illustrations of the PSD in the different points are provided in Figs. 10 – 13. For brevity, the presentation is restricted to the plane close to

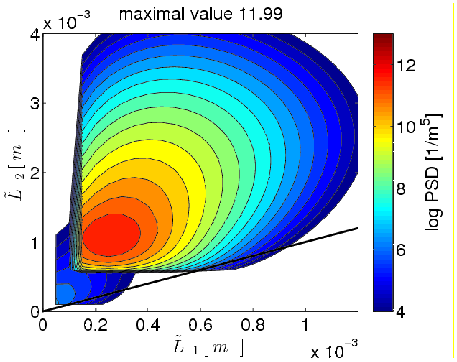

(a) $O = (200, 1/2, 1/2)$ cm, $\tilde{t}_{\max} = 240$ s

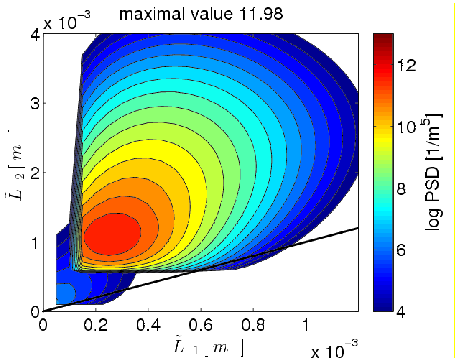

(b) $E = (200, 5/12, 1/2)$ cm, $\tilde{t}_{\max} = 245$ s

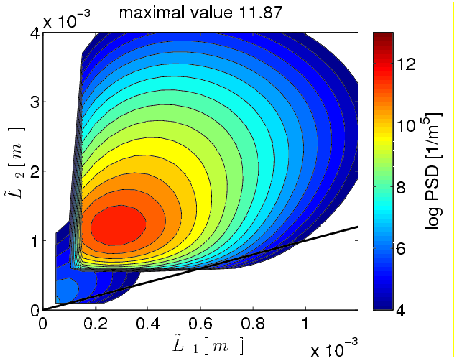

(c) $D = (200, 4/12, 1/2)$ cm, $\tilde{t}_{\max} = 264$ s

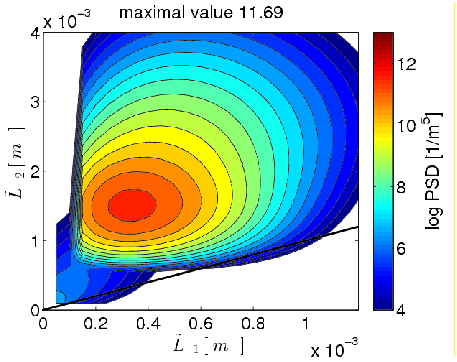

(d) $C = (200, 3/12, 1/2)$ cm, $\tilde{t}_{\max} = 300$ s

Fig. 10. Inflow rate $\tilde{V}_r = 30$ ml/min: (logarithm of the) PSD at $(200, \tilde{x}_2, \tilde{x}_3)$ cm, nodes on the line between the wall and the center; FWE-UPW-FDM. Note that at $A = (200, 1/12, 1/2)$ cm and $B = (200, 2/12, 1/2)$ cm there is no notable amount of particles predicted.

the outlet because the results at the outlet are of most interest. Details with respect to the other cut planes can be found in [27]. For each picture, the time instance is chosen where the maximal value of the PSD is obtained. It can be clearly observed that the results obtained with RK-ENO-FDM are much less smeared than the results computed with FWE-UPW-FDM. In addition, the maximal values of the PSDs are larger for RK-ENO-FDM. The smearing introduced by FWE-UPW-FDM results even in the fact that a notable amount of particles has already left the domain of computation for the internal coordinates at the end of the channel. In addition, there is also a certain amount of particles which are physically wrong since for them holds $\tilde{L}_1 > \tilde{L}_2$. For both methods, the results in the points close to the center of the channel are almost identical with the results in the center itself. Only the maximal value of the PSD is taken a little bit earlier at the center. Towards the walls, the amount of particles becomes smaller, to be negligible close to the walls. In the point C', see Figs. 12 and 13, the results are qualitatively different. The pictures in Figs. 10 – 13 also allow to distinguish between the part of the PSD that originates

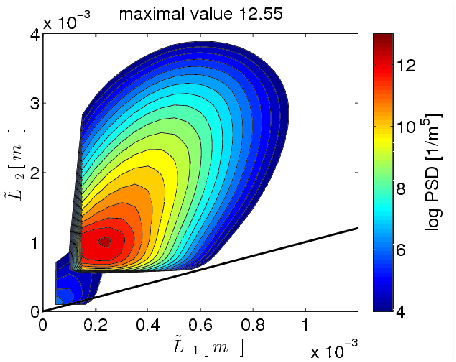

(a) $O = (200, 1/2, 1/2)$ cm, $\tilde{t}_{\max} = 240$ s

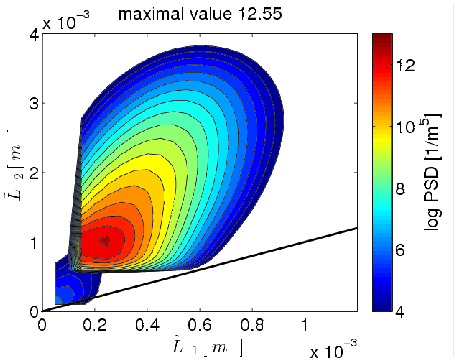

(b) $E = (200, 5/12, 1/2)$ cm, $\tilde{t}_{\max} = 245$ s

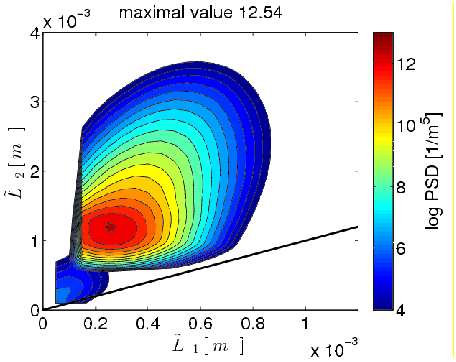

(c) $D = (200, 4/12, 1/2)$ cm, $\tilde{t}_{\max} = 264$ s

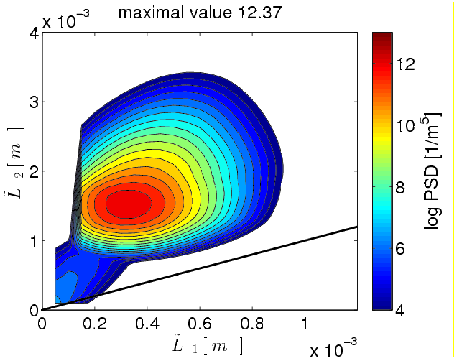

(d) $C = (200, 3/12, 1/2)$ cm, $\tilde{t}_{\max} = 300$ s

Fig. 11. Inflow rate $\tilde{V}_r = 30$ ml/min: (logarithm of the) PSD at $(200, \tilde{x}_2, \tilde{x}_3)$ cm, nodes on the line between the wall and the center; RK-ENO-FDM. Note that at $A = (200, 1/12, 1/2)$ cm and $B = (200, 2/12, 1/2)$ cm there is no notable amount of particles predicted.

from the inlet seed and the part which comes from the nucleation. Also for the latter part, the smearing introduced by FWE-UPW-FDM is clearly visible.

Differences in the numerical results can be seen also in other quantities of the population balance system. The final concentration fields computed with FWE-UPW-FDM and RK-ENO-FDM are depicted in Fig. 14. On the whole, both fields look similar, but they are actually different in details. A clear difference can be seen in the middle of the channel, at $\tilde{x}_1 \approx 100$ cm, toward the walls, where the concentration obtained with FWE-UPW-FDM is much smaller than the concentration computed by RK-ENO-FDM. Even more striking, the same situation can be observed at the end of the channel. The smaller values for FWE-UPW-FDM at the end of the channel arise from the fact that due to the smearing of this method larger particles are produced. For creating larger particles, more of the dissolved species has to be consumed, leading finally to smaller values for the concentration.

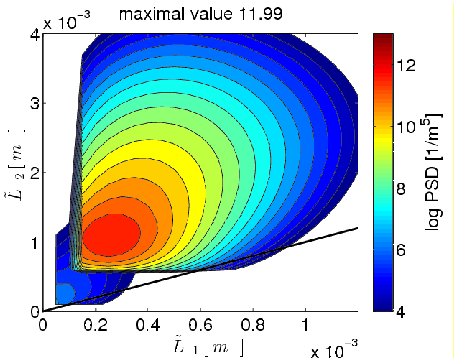

(a) $O = (200, 1/2, 1/2)$ cm, $\tilde{t}_{\max} = 240$ s

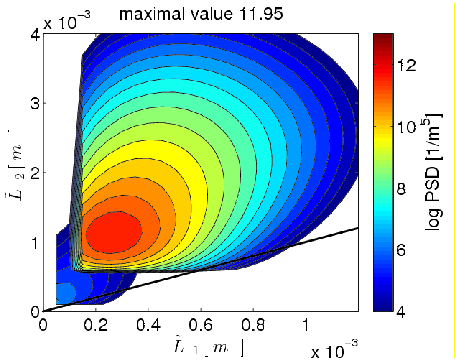

(b) $E' = (200, 5/12, 5/12)$ cm, $\tilde{t}_{\max} = 251$ s

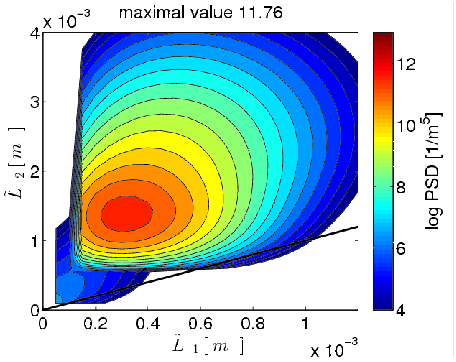

(c) $D' = (200, 4/12, 4/12)$ cm, $\tilde{t}_{\max} = 291$ s

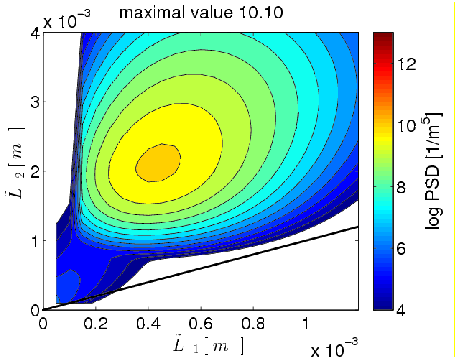

(d) $C' = (200, 3/12, 3/12)$ cm, $\tilde{t}_{\max} = 300$ s

Fig. 12. Inflow rate $\tilde{V}_r = 30$ ml/min: (logarithm of the) PSD at $(200, \tilde{x}_2, \tilde{x}_3)$ cm, nodes on the line between the corner and the center, FWE-UPW-FDM. Note that at $A' = (200, 1/12, 1/12)$ cm and $B' = (200, 2/12, 2/12)$ cm there is no notable amount of particles predicted.

5.2 Inflow rate 90 ml/min

A second study was performed with the inflow rate of $\tilde{V}_r = 90$ ml/min. For brevity, only a few results will be presented in this report, for a detailed evaluation of this study it is referred to [27].

The inflow rate $\tilde{V}_r = 90$ ml/min leads to a stationary flow field with Reynolds number $Re \approx 1044$. Since the flow is considerably faster than in the study from Section 5.1, the residence time of the particles is shorter. Consequently, there will be less time to achieve large particles by nucleation and growth compared with the study from Section 5.1.

It can be seen in the numerical simulations that after $\tilde{t} = 150$ s almost all particles had left the domain. Using the same methodology as in Section 5.1, it is found that $\Delta t = 0.025$ is an appropriate length of the time step in this

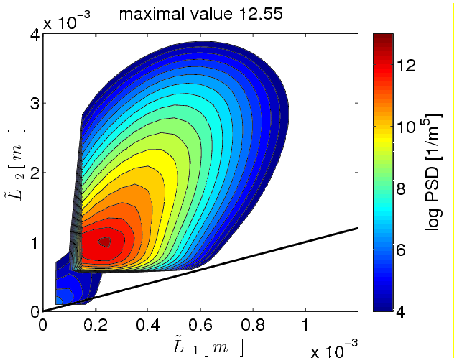

(a) $O = (200, 1/2, 1/2)$ cm, $\tilde{t}_{\max} = 240$ s

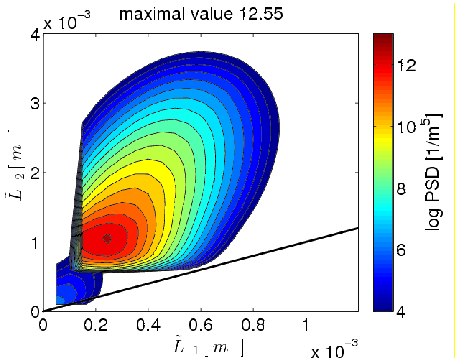

(b) $E' = (200, 5/12, 5/12)$ cm, $\tilde{t}_{\max} = 251$ s

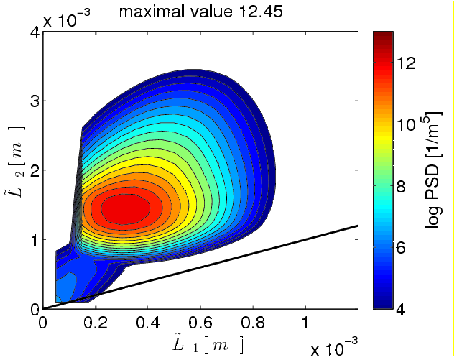

(c) $D' = (200, 4/12, 4/12)$ cm, $\tilde{t}_{\max} = 291$ s

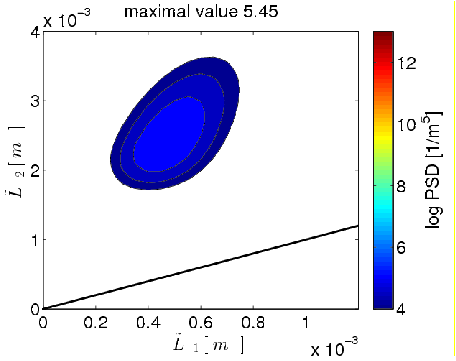

(d) $C' = (200, 3/12, 3/12)$ cm, $\tilde{t}_{\max} = 300$ s

Fig. 13. Inflow rate $\tilde{V}_r = 30$ ml/min: (logarithm of the) PSD at $(200, \tilde{x}_2, \tilde{x}_3)$ cm, nodes on the line between the corner and the center, RK-ENO-FDM. Note that at $A' = (200, 1/12, 1/12)$ cm and $B' = (200, 2/12, 2/12)$ cm there is no notable amount of particles predicted.

study, which is used in the simulations.

The evolution of the maximal value of the PSD for different nodes at the outlet is depicted in Fig. 15. Again, one can observe clear differences between the results obtained with FWE-UPW-FDM and with RK-ENO-FDM. For instance, considering the center of the channel, FWE-UPW-FDM predicts a notable amount of particles in the time interval $[60, 100]$ s, whereas RK-ENO-FDM predicts the same event in $[70, 90]$ s. The maximal amount of particles predicted by RK-ENO-FDM is almost twice as large as the prediction by FWE-UPW-FDM. Having a look at the PSD in the center of the outlet, Fig. 16, the much stronger smearing of FWE-UPW-FDM compared with RK-ENO-FDM can be observed well. Altogether, both methods give results which differ considerably in important properties. But the differences are smaller than for the study in Section 5.1. The same trend can be observed also for all other results. We think that the shorter residence time of the particles in the channel is the reason for the smaller differences.

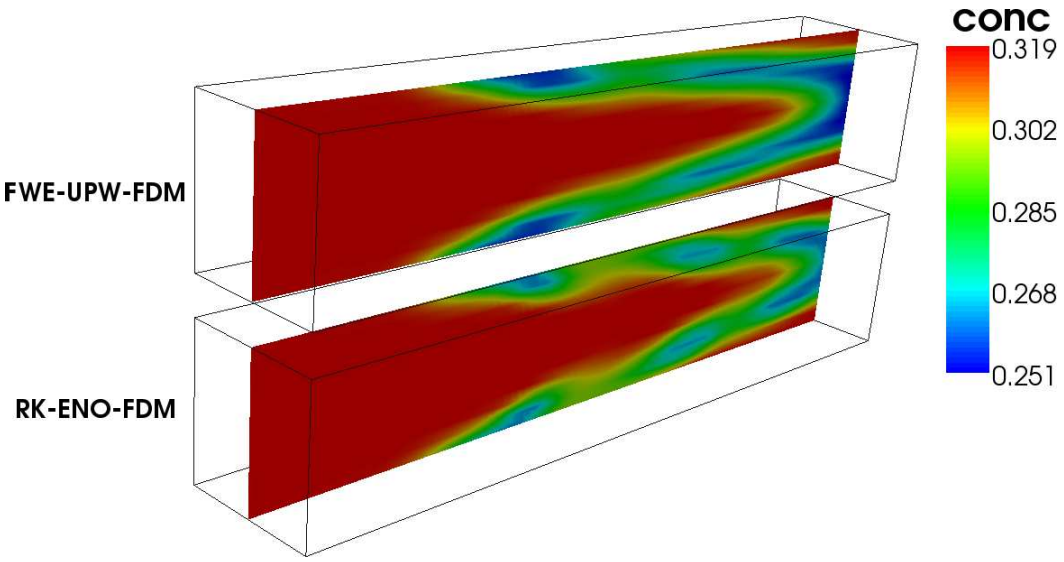

Fig. 14. Inflow rate $\tilde{V}_r = 30$ ml/min: final concentration field ($\tilde{t} = 300$ s) with FWE-UPW-FDM and RK-ENO-FDM, domain scaled by factor 40 in y- and z-direction.

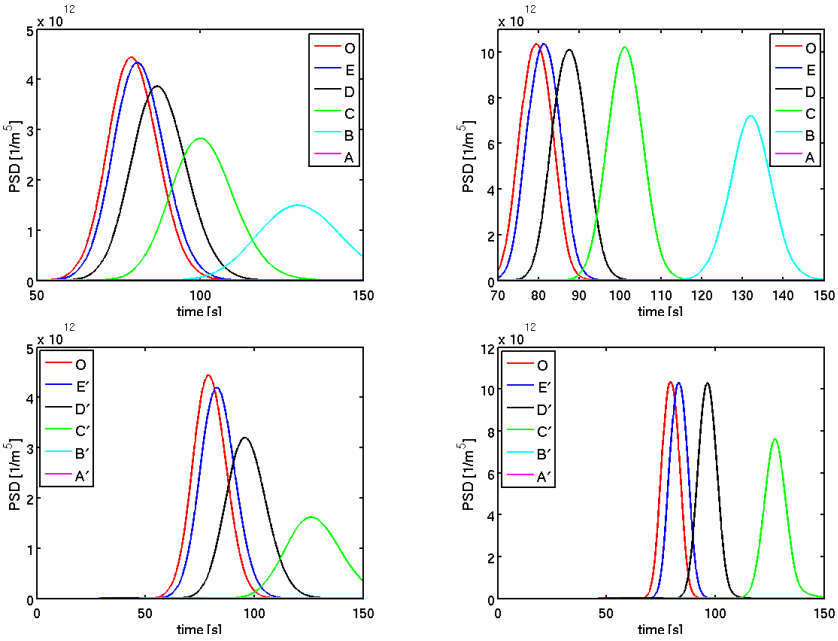

Fig. 15. Inflow rate $\tilde{V}_r = 90$ ml/min: maximal value of PSD at different nodes $(200, \tilde{x}_2, \tilde{x}_3)$ cm, FWE-UPW-FDM (left), RK-ENO-FDM (right). Note the different scaling of the y-axes. Maximal values of PSD in the nodes close to the wall (corner) are negligible (magenta, cyan curves).

5.3 Discussion and further aspects of the simulations

In this section, two direct discretizations of a bi-variate population balance system were studied, which differ only in the discretization of the differential

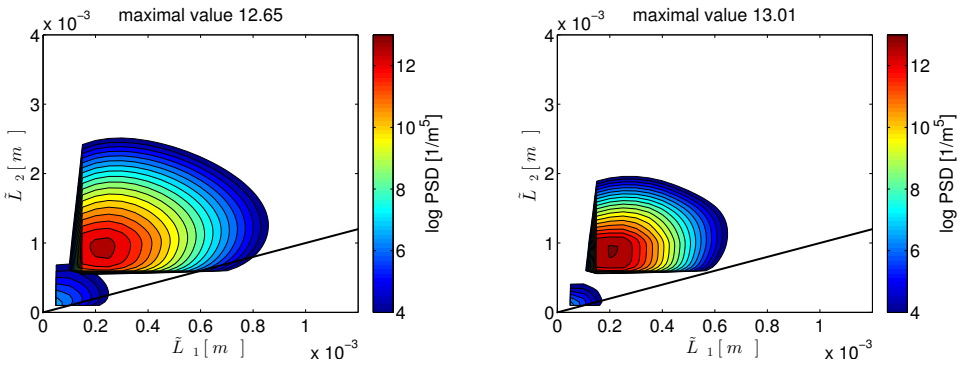

Fig. 16. Inflow rate $\tilde{V}_r = 90$ ml/min: (logarithm of the) PSD at $(200, 1/2, 1/2)$ cm, $\tilde{t}_{\max} = 79$ s, FWE-UPW-FDM (left), RK-ENO-FDM (right).

operator in the equation for the PSD. Since the solutions in the considered examples are smooth, it can be expected that the third order method RK-ENO-FDM gives more accurate results than the first order method FWE-UPW-FDM. For the time steps which were chosen to be appropriate, difficulties with spurious oscillations, which might generally arise in using RK-ENO-FDM, did not occur.

Both methods predicted that the bulk of the particles follows the flow field very well, i.e., most of the particles stay in the center of the channel and much less particles can be found closer to the walls. In all simulations, the computed PSDs at the outlet allow to distinguish clearly the contributions coming from the seed at the inlet and coming from the nucleation. Apart from these general agreements, there are considerable differences between the results computed with FWE-UPW-FDM and RK-ENO-FDM. The solutions computed with RK-ENO-FDM are considerably less smeared compared with the the solutions obtained using FWE-UPW-FDM. A notable amount of particles at the outlet is predicted by RK-ENO-FDM in time intervals that are only half as long as the time intervals predicted by FWE-UPW-FDM. In addition, the maximal value of the PSD was two to four times larger for RK-ENO-FDM. Altogether, these results are quantitatively much different. The numerical studies show also that the differences between the results obtained with the two methods become larger the longer the residence time of the particles is.

The simulations were performed with the code MooNMD [15] on HP BL2x220c computers with 2933 MHz Xeon processors. Simulating one time step for FWE-UPW-FDM took around 30 seconds, including the calculation of all data for evaluating the numerical simulations. The method RK-ENO-FDM had higher computational cost, in our simulations of around a factor of five.

6 Summary and outlook

This report presented numerical studies of two methods for simulating a bivariate population balance system, modeling growth and nucleation of particles. Both methods differed only in the discretization of the differential operator of the population balance equation, where both discretizations belonged to the class of direct discretizations (discrete methods). One method applied a monotone first order discretization (FWE-UPW-FDM) whereas the other one used an essentially non-oscillatory third order discretization (RK-ENO-FDM). The main goal of the simulations consisted in studying the accuracy of the numerical results. It turned out that important quantities of interest, like the maximal value of the PSD at the outlet or the time interval in which a notable amount of particles passed the outlet, were predicted much differently by both methods. It was discussed in Section 5.3 that the results computed with the higher order method can be considered to be more accurate.

As discussed in the introduction, the choice of a numerical method for a simulation should depend on the goal of that simulation. From the results presented in this report, we draw the conclusion to use as accurate methods as affordable if, e.g., the detailed study of a population balance system is of interest. For such purposes, it is more beneficial to get an accurate solution after a longer (but affordable) computing time than to obtain an inaccurate solution in a short time.

Of course, also the efficiency of accurate (higher order) methods has to be studied and improved. From the point of view of implementation, parallelization might help considerably. With respect to population balance systems, the potential of other approaches, like moment-based methods or operator-splitting schemes, has to be studied for computing similarly or even more accurate solutions in a more efficient way than the used direct discretizations. To our best knowledge, the investigation of this topic is widely open and we plan to pursue it in our future work.

References

[1] C. Borchert. *Topics in Crystal Shape Dynamics*. PhD thesis, Otto–von–Guericke–Universität Magdeburg, 2012.

[2] C. Borchert and K. Sundmacher. Crystal aggregation in a flow tube: Image-based observation. *Chemical Engineering & Technology*, 34(4):545–556, 2011.

[3] Richard D. Braatz, David L. Ma, Mitsuko Fujiwara, and Rudiyanto Gunawan. Identification of kinetic parameters in multidimensional crystallization processes. *International Journal of Modern Physics B*, 16(01n02):367–374, 2002.

[4] A. Buffo, M. Vanni, D.L. Marchisio, and R.O. Fox. Multivariate quadrature-based moments methods for turbulent polydisperse gas–liquid systems. *International Journal of Multiphase Flow*, 50(0):41 – 57, 2013.

[5] L.G.M. de Souza, G. Janiga, V. John, and D. Thévenin. Reconstruction of a distribution from a finite number of moments with an adaptive spline-based algorithm. *Chem. Eng. Sci.*, 65(9):2741 – 2750, 2010.

[6] Sashikumaar Ganesan. An operator-splitting Galerkin/SUPG finite element method for population balance equations: stability and convergence. *ESAIM Math. Model. Numer. Anal.*, 46(6):1447–1465, 2012.

[7] Sashikumaar Ganesan and Lutz Tobiska. An operator-splitting finite element method for the efficient parallel solution of multidimensional population balance systems. *Chem. Eng. Sci.*, 69(1):59 – 68, 2012.

[8] A. Gerstlauer. *Herleitung und Reduktion populationsdynamischer Modelle am Beispiel der Flüssig-Flüssig-Extraktion*, volume 3 of *Verfahrenstechnik*. VDI Verlag, Düsseldorf, 1999.

[9] P.M. Gresho and R.L. Sani. *Incompressible Flow and the Finite Element Method*. Wiley, Chichester, 2000.

[10] Wolfgang Hackbusch, Volker John, Aram Khachatryan, and Carina Suciu. A numerical method for the simulation of an aggregation-driven population balance system. *Internat. J. Numer. Methods Fluids*, 69(10):1646–1660, 2012.

[11] Ami Harten, Björn Engquist, Stanley Osher, and Sukumar R. Chakravarthy. Uniformly high-order accurate essentially nonoscillatory schemes. III. *J. Comput. Phys.*, 71(2):231–303, 1987.

[12] C. Hirsch. *Numerical Computation of Internal and External Flows*, volume 1 of *Fundamentals of Computational Fluid Dynamics*. John Wiley and Sons, Chichester, 1988.

[13] H.M. Hulburt and S. Katz. Some problems in particle technology: A statistical mechanical formulation. *Chem. Eng. Sci.*, 19(8):555 – 574, 1964.

[14] V. John, I. Angelov, A.A. Öncül, and D. Thévenin. Techniques for the reconstruction of a distribution from a finite number of its moments. *Chem. Eng. Sci.*, 62(11):2890 – 2904, 2007.

[15] Volker John and Gunar Matthies. MooNMD—a program package based on mapped finite element methods. *Comput. Vis. Sci.*, 6(2-3):163–169, 2004.

[16] Volker John, Teodora Mitkova, Michael Roland, Kai Sundmacher, Lutz Tobiska, and Andreas Voigt. Simulations of population balance systems with one internal coordinate using finite element methods. *Chem. Eng. Sci.*, 64(4):733 – 741, 2009.

[17] Volker John and Julia Novo. On (essentially) non-oscillatory discretizations of evolutionary convection-diffusion equations. *J. Comput. Phys.*, 231(4):1570–1586, 2012.

[18] Volker John and Michael Roland. On the impact of the scheme for solving the higher dimensional equation in coupled population balance systems. *Internat. J. Numer. Methods Engrg.*, 82(11):1450–1474, 2010.

[19] Volker John and Ellen Schmeyer. Finite element methods for time-dependent convection-diffusion-reaction equations with small diffusion. *Comput. Methods Appl. Mech. Engrg.*, 198(3-4):475–494, 2008.

[20] Volker John and Ellen Schmeyer. On finite element methods for 3D time-dependent convection-diffusion-reaction equations with small diffusion. In *BAIL 2008—boundary and interior layers*, volume 69 of *Lect. Notes Comput. Sci. Eng.*, pages 173–181. Springer, Berlin, 2009.

[21] Dmitri Kuzmin. Explicit and implicit FEM-FCT algorithms with flux linearization. *J. Comput. Phys.*, 228(7):2517–2534, 2009.

[22] D.L. Ma and R.D. Braatz. Worst-case analysis of finite-time control policies. *Control Systems Technology, IEEE Transactions on*, 9(5):766–774, 2001.

[23] Aniruddha Majumder, Vinay Kariwala, Santosh Ansumali, and Arvind Rajendran. Lattice boltzmann method for multi-dimensional population balance models in crystallization. *Chem. Eng. Sci.*, 70(0):121 – 134, 2012.

[24] Daniele L. Marchisio and Rodney O. Fox. Solution of population balance equations using the direct quadrature method of moments. *Journal of Aerosol Science*, 36(1):43 – 73, 2005.

[25] Robert McGraw. Description of aerosol dynamics by the quadrature method of moments. *Aerosol Science and Technology*, 27(2):255–265, 1997.

[26] Chi-Wang Shu. High order weighted essentially nonoscillatory schemes for convection dominated problems. *SIAM Rev.*, 51(1):82–126, 2009.

[27] C. Suciu. *Numerical methods based on direct discretizations for uni- and bi-variate population balance systems*. PhD thesis, Freie Universität Berlin, Fachbereich Mathematik und Informatik, 2013.

[28] Timokleia Togkalidou, Mitsuko Fujiwara, Shefali Patel, and Richard D Braatz. Solute concentration prediction using chemometrics and atr-ftir spectroscopy. *Journal of Crystal Growth*, 231(4):534 – 543, 2001.